Constitutive modeling of a graded porous polymer based on X-ray computed tomography

Ole Vestrum [a,b,*], Lars Edvard Blystad Dæhli [a], Odd Sture Hopperstad [a,b], Tore Børvik [a,b]

[a] Structural Impact Laboratory (SIMLab), Department of Structural Engineering, Norwegian University of Science and Technology (NTNU), NO-7491 Trondheim, Norway
[b] Centre for Advanced Structural Analysis (CASA), NTNU, NO-7491 Trondheim, Norway

HIGHLIGHTS

- Porous polymer pipeline coating sample was scanned using X-ray micro CT.
- FE models representing the actual pore morphology were produced.
- The yield strength was mapped across the coating using unit cell analyses.
- A constitutive model framework was proposed and implemented in Abaqus.

GRAPHICAL ABSTRACT
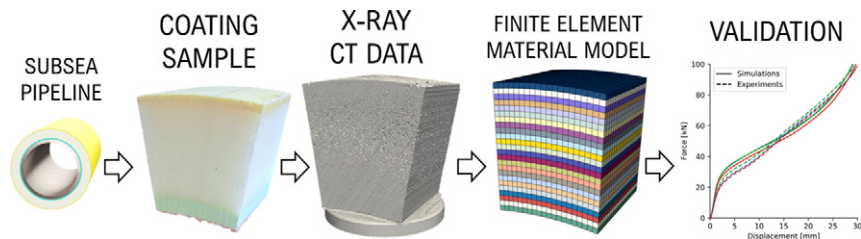
ABSTRACT

This work focuses on the constitutive modeling of a graded porous polymer pipeline coating based on X-ray micro computed tomography (XRMCT). Previous work has revealed that finite element (FE) models generated from XRMCT scans of cylindrical coating specimens reproduce their response in uniaxial compression accurately. In this work, we use FE models generated from XRMCT scans to study the pressure-sensitive yield strength of the porous coating. Since the coating is known to have a graded pore structure through its thickness, data from an XRMCT scan of a full coating sample is divided into twenty-four sublayers across the coating thickness, from which FE models are generated. These FE models are used to perform numerical limit analyses to map the yield locus for each sublayer, which are utilized to calibrate an analytical yield surface. A strong correlation is found between the fitted yield surface parameters and the average porosity of the sublayers. This observation is used to propose a constitutive model where the yield strength depends on the porosity and its evolution with deformation. The constitutive model is implemented as a user subroutine in a commercial explicit FE solver and validated against experimental component tests, showing good agreement.

1. Introduction

Steel pipelines are used to transport hydrocarbon fluids along the seabed. To preserve the inherent temperature of the fluid flow, thus preventing the formation of hydrocarbon precipitates and loss of pressure, pipelines are often coated with insulating polymeric coating systems [1]. These coatings have been shown to influence the mechanical response of the subsea pipelines. There exists a great economic potential

* Corresponding author at: Structural Impact Laboratory (SIMLab), Department of Structural Engineering, Norwegian University of Science and Technology (NTNU), NO-7491 Trondheim, Norway
E-mail address: ole.vestrum@ntnu.no (O. Vestrum).

in including polymeric coating products in the structural analysis of a full pipeline design with respect to reduced material consumption in more optimized cross-sectional designs and more efficient pipeline routes. The prevailing standards allow the inclusion of beneficial contributions made by coatings to the structural integrity of pipeline designs, but any possible effects need to be documented [2]. Such documentation is sought through either comprehensive experimental test programs, numerical analyses, or a combination of both. While the experiments are often expensive, time-consuming and case-specific, numerical simulations serve as a potentially cost-effective, time-efficient and versatile alternative. However, the complex designs of polymeric coatings complicate the use of standardized numerical approaches and make it difficult to include them in modern computational frameworks – such as the finite element (FE) method. Much effort has been devoted to estimating the mechanical response of anti-corrosion coatings [3,4], but certain features of pipeline insulation solutions further complicate the use of common modeling techniques. Porous materials are commonly used in such solutions due to their superior thermal properties [5], but these materials are at the same time found to contribute considerably to the structural capacity of pipelines [6] under extreme loading conditions such as accidental impact loads. A porous material is understood to be a two-phase material made up of a solid material with a distributed pore phase. The separation of the pores and the solid material is in general made on the macroscopic scale, while the morphological features of the solid polymer are considered on the microscopic scale. According to Gibson and Ashby [7], cellular solids are governed by the geometrical features (i.e., macroscopic features) of the pores and the intrinsic properties of the solid phase material (i.e., microscopic features). The properties of a cellular solid are often modeled as a function of the properties of the constituent material scaled with the porosity. Reyes and Børvik [8] performed uniaxial compression tests on specimens made of foamed extruded polystyrene and expanded polypropylene at three different densities each. They found a clear correlation between specimen density, and the stiffness and strength of the materials. Vestrum et al. [9] also revealed that the porous morphology found in these polymer-based coatings dominates the mechanical behavior. It follows that there exists a need for an effective modeling framework for porous coating products.

X-ray micro computed tomography (XRMCT) has proved itself as a viable tool in deriving FE meshes of the actual macroscopic morphology of cellular materials [10–14]. In previous work by Vestrum et al. [9], the macroscopic and microscopic morphologies in a series of porous polymer coating specimens were mapped using XRMCT and differential scanning calorimetry. Finite element meshes of the actual porous structures were derived from the XRMCT data. All specimens were also experimentally tested in uniaxial compression and used in the validation of the modeling approach. The approach was found to reproduce the mechanical behavior across a wide range of specimen morphologies. However, due to the computational requirements of conducting such analyses, alternative modeling methods are deemed necessary to investigate the mechanical behavior of full-scale components. The XRMCT-based framework is thought to serve as a means in the development of constitutive models.

In the framework proposed by Vestrum et al. [9], the porous pipeline material was directly modeled using a fine mesh of finite elements. As the final goal is to run FE simulations of real components using this approach, the number of elements must be reduced. Thus, a constitutive model, which represents the mechanical behavior of larger coating volumes, must be developed. Many different materials are known to have mechanical properties that are sensitive to the hydrostatic stress (i.e., pressure), such as the yield strength [15–18]. While the von Mises yield criterion [19] is invariant to the hydrostatic stress and only a function of the deviatoric part of the stress tensor, other criteria allow for yielding to occur under pure hydrostatic stress states. Drucker and Prager [15] introduced a pressure-dependent yield criterion for describing the plastic deformation of soils, which has also been applied to

concrete, polymers and foams. Deshpande and Fleck [18] presented an isotropic yield function derived from phenomenological observations, which has become a much-used model for cellular materials. Gurson [16] developed a model intended for porous ductile materials with much lower void (cell) volume fractions than in foams. The Gurson yield criterion [16] has a shape comparable to that proposed by Deshpande and Fleck [18], but is derived through an intricate evaluation of a small hollow sphere in a rigid-perfectly plastic material. Fritzen et al. [20] presented a homogenization procedure for estimating the effective global yield function by considering a fictious porous solid on three scales. FE models of representative volume elements were generated, where the solid phase was modeled as plastically compressible (i.e., pressure sensitive) and porosity was produced by eroding perfect spherical shapes. Using unit cell simulations on these FE models, the authors mapped the global yield surface. The idea presented by Fritzen et al. [20] has fundamental similarities to the approach presented in this work, but the models used here are derived from actual material specimens and the applied constitutive models differ.

In this work, a model for the constitutive behavior of a graded porous polymer pipeline coating is proposed. To this end, a framework is established where XRMCT is used to characterize and model the macroscopic structure. The aim of the work is to establish a constitutive model for the elastic-plastic behavior of the coating material. An XRMCT scan of a large coating specimen is used as a means for the approach. FE models of the macroscopic structure are produced to analyze how the initial yield strength varies across the coating. The results from these analyses are used to establish a constitutive model for the coating material. Fig. 1 provides an overview of the essential steps in the approach for deriving a validated constitutive model. The figure also indicates the sections where the different steps are introduced. Section 2 presents the multi-layer polymer coating studied in this work. Section 3 contains details related to the acquisition and post-processing of the data produced by the XRMCT scan of the coating sample. The XRMCT data is post-processed to facilitate both quantitative characterization of the macroscopic pore structure and the conversion to FE models. Previous work has revealed an inhomogeneous macroscopic morphology across the thickness of the coating. Here, the XRMCT data is sectioned into 24 smaller volumes (called sublayers) across the thickness. FE models are derived from each of these sublayers. A unit cell framework [21] is then used to study the influence of the macroscopic structure on the pressure sensitivity of the yield strength of each sublayer. Pointwise numerical limit analyses mapping the initial yield surface in terms of the von Mises equivalent stress and the hydrostatic stress are finally performed for each sublayer. In Section 4, the Deshpande-Fleck yield function for cellular materials is calibrated to these mappings to develop an elastic-plastic constitutive model to be used in full-scale FE analysis. A strong correlation between the parameters of the yield function and the macroscopic porosity of the sublayers is found. This correlation is used to make the parameters of the Deshpande-Fleck yield function dependent on and evolving with the porosity of the material element. The elastic-plastic constitutive model of the polymer coating is implemented as a material subroutine in Abaqus/Explicit [22] and validated against experimental compression tests of coating specimens in Section 5. The novel aspect of this work is a modeling framework for porous solids based on numerical limit analyses of the actual macroscopic morphology using XRMCT imaging. In this study, the framework was used to establish a constitutive model for a porous polymer pipeline coating. The parameters are correlated with the coating porosity, which allows the model response to evolve with the changes in the macroscopic morphology as the material deforms.

2. Material

A typical multi-layer polypropylene-based coating system found on rigid steel pipelines in the North Sea is considered in this study. The coating is a commercial product known as Thermotite and produced by
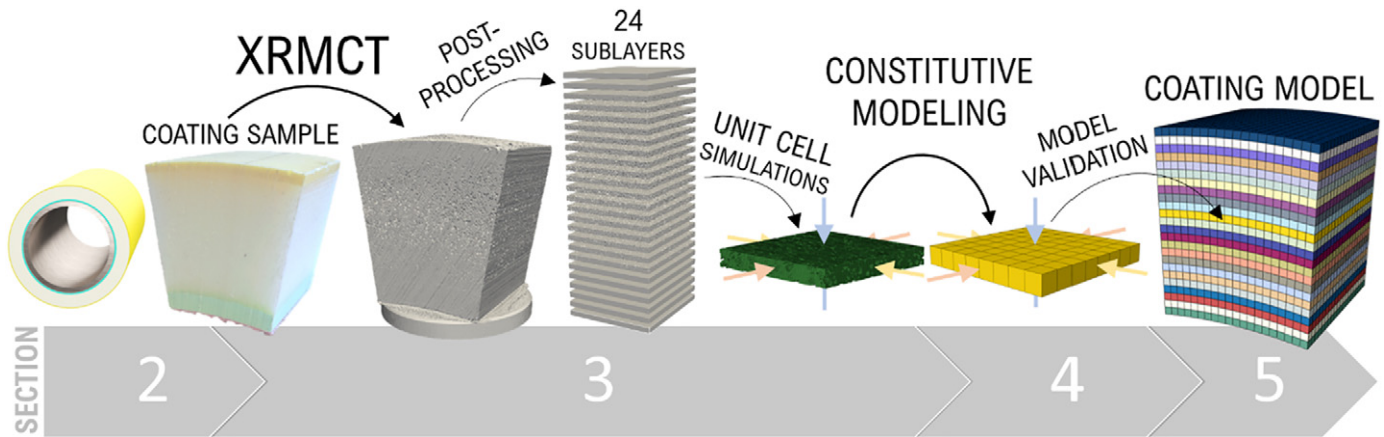
Fig. 1. Overview of the various modeling steps.

Shawcor Norway [23]. Such coatings may come in a range of layer configurations and thicknesses to serve different application demands. This customizability results in a wide range of designs with often very different properties. Fig. 2(a) presents a rendering of a pipeline sample with the coating design investigated in this study, while Fig. 2(b) gives a detailed overview of layer dimensions and features over the cross-section. The latter figure also introduces a polar coordinate system that is used throughout the article. Each individual layer in the full coating system serves a unique purpose. While the innermost layers (3LPP in Fig. 2(b)) are in themselves a common anti-corrosion solution for pipelines, this coating system also has two additional external layers providing thermal insulation. The porous layer consists of a polypropylene material produced by the Borealis Group called BA202E [24] and constitutes over 80% of the total coating thickness. Examinations of the same coating system have documented significant gradients in density, which is closely related to the mechanical properties, throughout the thickness of the porous layer [6,9]. This was reasoned to be caused by morphological gradients on both the micro- and macroscopic scales within the coating material [9]. In this work, we investigate the influence of the macroscopic morphology on the mechanical behavior of the coating.

3. XRMCT-based modeling

3.1. Experimental work

In this study, we use XRMCT to produce 3D images of the macroscopic porous morphology of the coating. XRMCT is a nondestructive imaging technology for mapping densities in 3D volumes at discrete points of micrometer scale. In typical industrial XRMCT, a series of X-ray radiographs is sampled over a given volume at different angles as the specimen rotates on a rotary mount. Each radiograph is a two-dimensional (2D) gray-scale image representing the attenuation of radiation of the mass occupying the volume. By correlating all the radiographs, a 3D image may be reconstructed. Each discrete point in the 3D image, called a voxel (equivalent to a 2D pixel), holds a gray-scale value. As the attenuation of X-ray radiation is a function of material density, the gray-value of a voxel is related to the mass density of the subspace it covers.

A single specimen of the same coating as described in Section 2 was retrieved from actual subsea pipeline samples and consisted of all polymeric layers as presented in Fig. 2(b). The specimen was arch-shaped
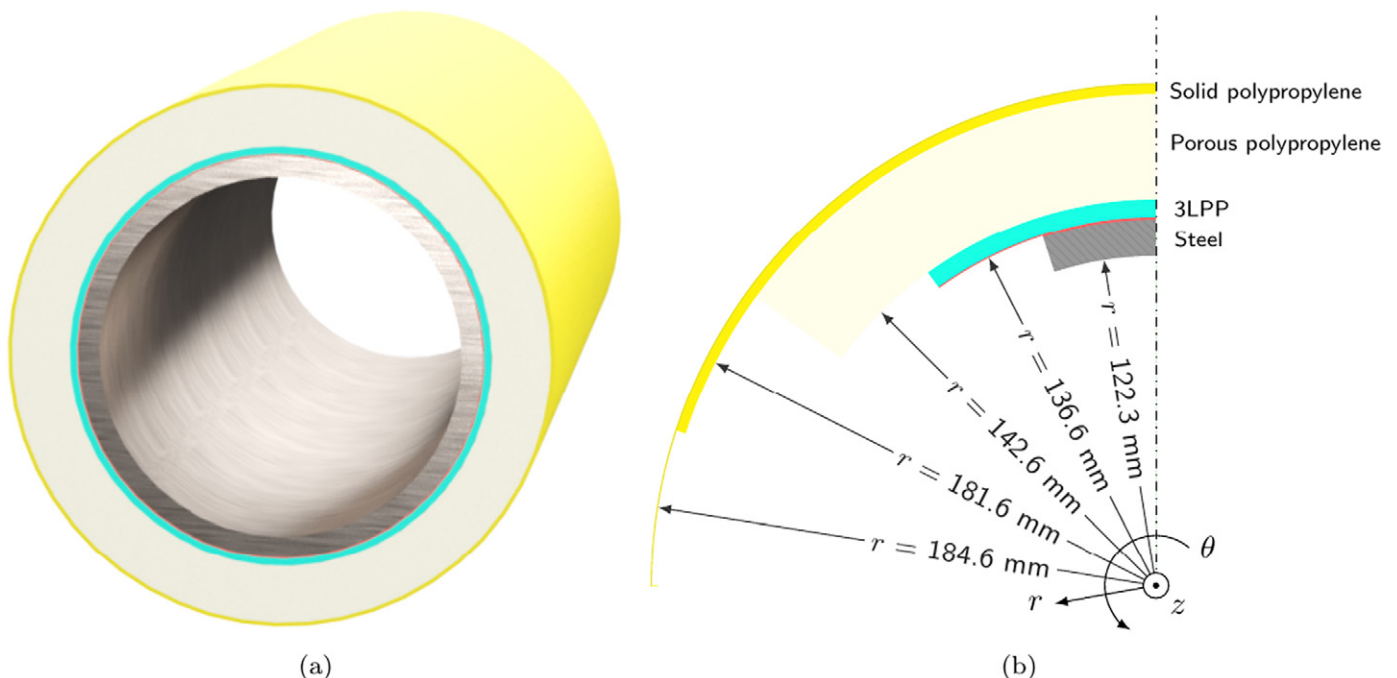

Fig. 2. (a) Illustrative overview and (b) cross-section (with dimensions) of the studied pipeline design.

with approximate minimum length spans along the z, θ and r directions of 40 mm, 35 mm and 48 mm, respectively (see Fig. 3(a)). As the supplied pipeline sample had no obvious markings that indicates its extrusion direction, the positive direction of the z-axis was chosen arbitrarily. The specimen was scanned using a Nikon XT H225 ST MicroCT machine at the Norwegian University of Science and Technology (NTNU). Fig. 3 (b) presents a picture of the setup inside the machine. This is a laboratory XRMCT device with a 225 kV Wolfram reflection target (X-ray source in Fig. 3(b)), and a panel detector with 2000×2000 pixels of 200 µm pixel size and 16-bit pixel depth (X-ray detector in Fig. 3(b)). To reduce the accumulation of random noise, every single projection was produced by averaging two separate X-ray radiographs (each with 1 s exposure time). A total of 1751 projections were produced during a full rotation of the specimen. After the scan was completed, the volume was reconstructed using the commercial software Nikon CT Pro 3D (Version XT 3.1.3). The 3D density mapping was then exported as a series (stack) of 8-bit gray-scale images. Each image represents a cross-section of the volume with the same spatial thickness as the pixels in the image, giving a set of (cubic) voxels. The metadata produced by the reconstruction software reported a voxel resolution of 0.0351 mm $\times$ 0.0351 mm $\times$ 0.0351 mm. Fig. 3(c) shows a surface rendering produced from the exported image stack. As the raw data consists of 8.0×10^9 voxels, the 3D voxel matrix needs to be processed to make it eligible for further characterization and model adaptation.

3.2. Post-processing

While the raw data produced by XRMCT may provide qualitative insight to some of the coating features, it needs to be further processed to facilitate its use in the simulation framework [9]. The raw data is essentially a 3D matrix ($2000 \times 2000 \times 2000$ voxels) where each entry holds an 8-bit integer (i.e., a discrete value from 0 to 255), which represents each voxel and the radiodensity of the subspace it spans. The raw data is referred to as a voxel matrix in the sequel. The following section presents an overview of the post-processing steps necessary to establish the finite element models. For a fully detailed description of the FEA preparation process, the reader is referred to Vestrum et al. [9]. Except for the acquisition and reconstruction of the raw XRMCT data, all the post-processing steps were conducted using open-license software and freely available Python modules.

As the specimen originates from a pipeline cross-section with a curvilinear coordinate system (as presented in Fig. 2(b)), the raw voxel matrix is transformed to fit a Cartesian coordinate system to ease further processing. By fitting circular shapes to the innermost curvature of the *3LPP* layers (red dashed line in Fig. 4(a)) and the outmost curvatures

of the *Solid polypropylene* layer (black dashed line in Fig. 4(a)), and utilizing their known spatial values, the polar axis of the polar coordinate system was estimated. After establishing the polar axis, the scalar field was evaluated at intermediate radial values (at intervals corresponding to a voxel's span along r) to create a flattened representation as illustrated in Fig. 4(b). The Cartesian coordinate axes were denoted r^*, θ^* and z^*, and the transformed data set was cropped to remove artifacts caused by machining processes and assuring straight boundary walls. The dimensions of the matrix (after cropping) are described by $r_0^* \times \theta_0^* \times z_0^*$ equaling $1374 \times 954 \times 1063$ voxels that spans 48.2 mm $\times$ 33.5 mm $\times$ 37.3 mm. This remapped voxel matrix is used as basis for the FEA preparation process.

The model preparation steps described in detailed by Vestrum et al. [9] are applied to the cropped voxel matrix in order to convert the data to FE meshes. While a full restatement of the procedure is omitted herein, a brief outline is provided in the following. Owing to the high resolution produced by the XRMCT, a downscaling is necessary to make the final FE models computationally tractable. Vestrum et al. [9] found, through the analyses of cylindrical specimens with height 6 mm and diameter 10 mm, that a downscaled version of the voxel matrix with element corresponding to side lengths of 0.08 mm produced very good results in terms of model run time and correspondence with experimental results. This downscaling implies a reduction of spatial resolution by a factor of 2.28 ($=0.08/0.0351$) for the respective voxel matrix. In addition to downscaling, a key step in the preparation is to make a clear distinction between polymer and pores through a segmentation process known as binarization. Binarization entails deciding on a gray value threshold, which divides the voxel matrix' bimodal gray scale histogram into two and separates solid and non-solid matter. The binary voxel matrix represents a 3D image of the macroscopic morphology found in the coating sample, and it is this data set that is used as the basis for deriving the sublayer models in the next section.

3.3. Sublayer models

In this section, we present the steps taken in evaluating the pressure sensitivity of the yield strength introduced by the macroscopic morphology across the coating thickness. The XRMCT-based modeling approach applied by Vestrum et al. [9] was used on the binary voxel matrix to derive FE models representing the macroscopic structure of thin layers throughout the coating thickness denoted sublayers. The sublayers were produced by slicing the voxel matrix into a total of 24 pieces along the radial direction. Each sublayer had a thickness of approximately 2 mm. The sublayers were analyzed using a FE unit cell model where the influence of the macroscopic morphology on the
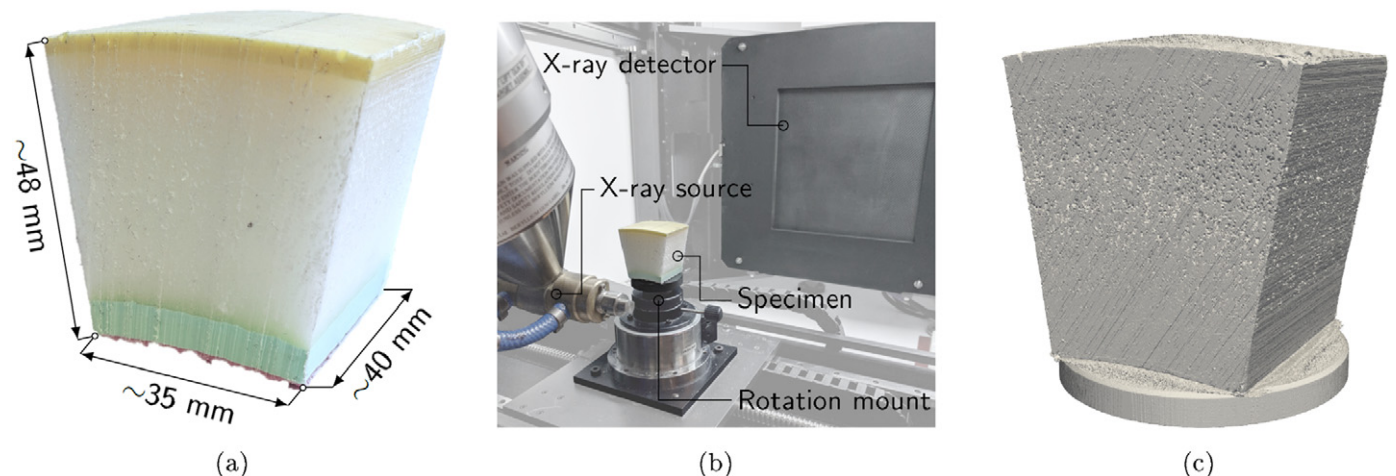

(a)   (b)   (c)

Fig. 3. Photos of (a) the coating specimen with approximate dimensions, (b) the setup inside the XRMCT machine and (c) a surface rendering of the scanned specimen and parts of the rotation mount.
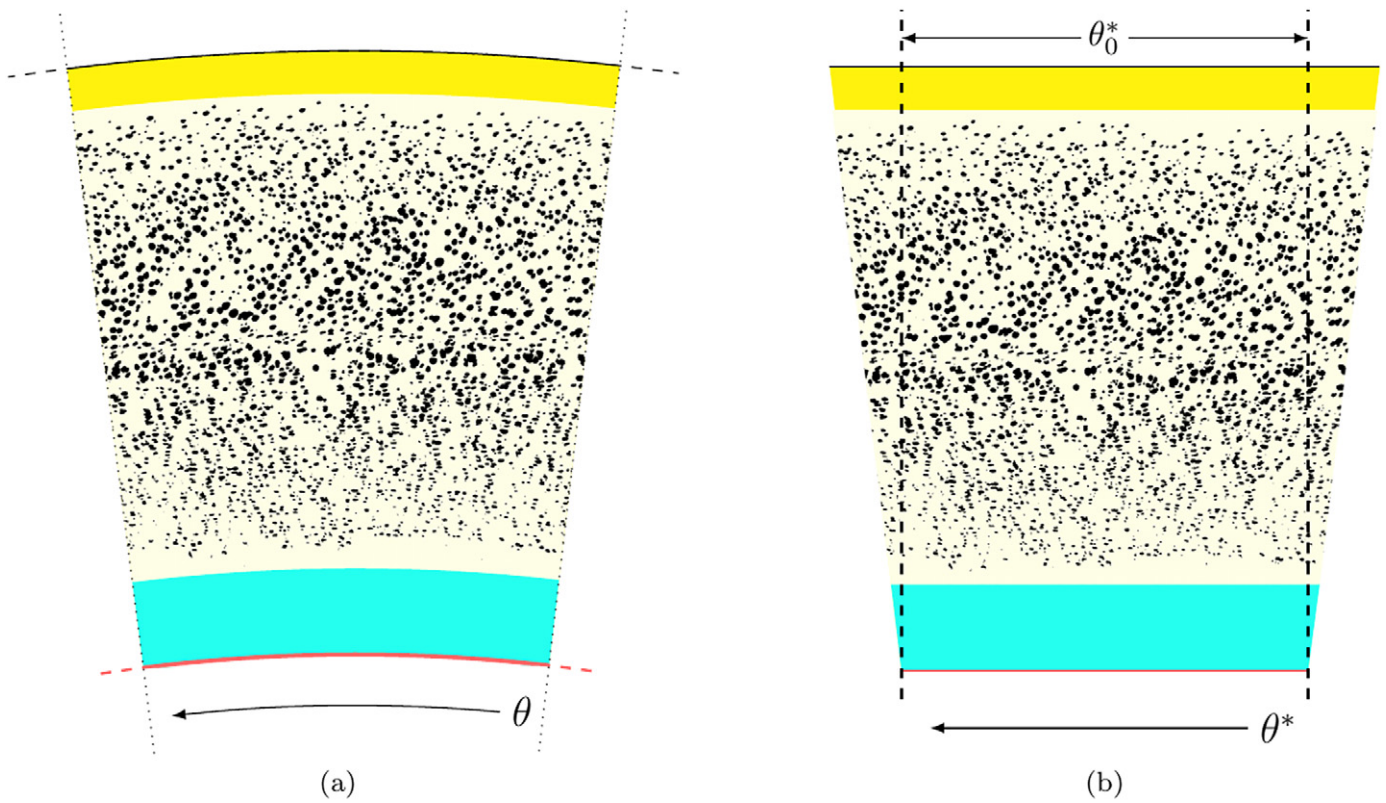
Fig. 4. Illustrations of the transformation from (a) a polar to (b) a Cartesian coordinate system.

yield strength of each sublayer region was analyzed. This procedure will be described in the subsequent sections. From visual observations of the voxel matrix, a preferred orientation in the macroscopic morphology is seen, which will inevitably influence the mechanical behavior of the sublayers [25]. The anisotropy is inherently captured by the unit cell model. However, to limit the scope of this work, we have not focused on assessing the anisotropic properties of the material, and we have consequently not investigated the effects of changing the principal loading direction in the numerical unit cell analyses. The choice of principal loading direction is justified by considering that the typical pipeline application usually entails compressive loading in the thickness (or r)

direction. Due to limitations in computational resources, ¼ of the voxel matrix was used to produce sublayer models with dimensions of around 16 mm $\times$ 16 mm $\times$ 2 mm. Elements with dimensions 0.08 mm $\times$ 0.08 mm $\times$ 0.08 mm have been shown to provide a good trade-off between model accuracy and runtime [9], and the same element size was chosen here.

Fig. 5 presents an overview of the analyzed sublayer models. Each sublayer model consisted of a unique FE mesh that is identified by the solid lines in Fig. 5(a) and given a number between 0 and 23 denoting to their position along r^*. The sublayer numbers 0, 1, 2 and 23 are left out of the FE modeling herein as they are free from pores and their
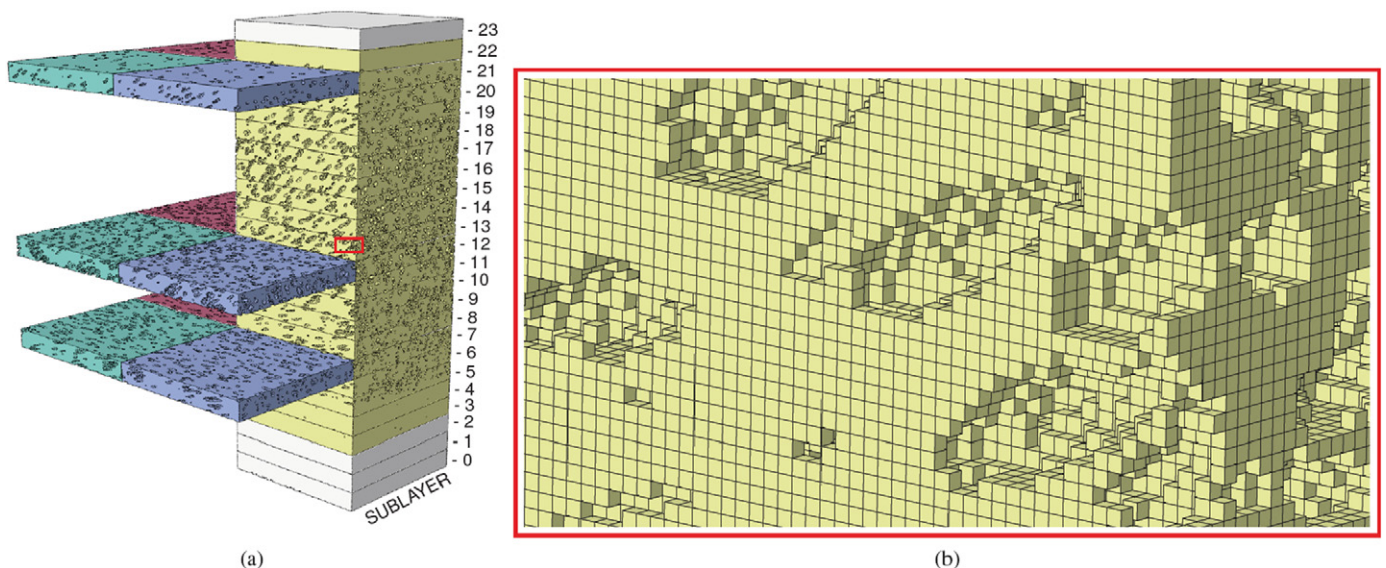

Fig. 5. (a) Overview and (b) close-up of geometries retrieved from the voxel matrix and used in the unit cell analyses.

mechanical behavior consequently conform to that of the polymer matrix. A full through-thickness evaluation (i.e., all permissible sublayers) was only performed on a quarter section of the voxel matrix (yellow volumes in Fig. 5). However, the remaining 3 quarters of the voxel matrix were also analyzed for sublayers 7, 12 and 21 to study the repeatability of the approach.

To aid the presentation of the results, normalized Cartesian coordinates $(\overline{r}^*, \overline{\theta}^*, \overline{z}^*) \in [0, 1]$ are defined as

$$\overline{r}^* = \frac{r^* - \Delta r^*}{r_0^*}, \quad \overline{\theta}^* = \frac{\theta^*}{\theta_0^*}, \quad \overline{z}^* = \frac{z^*}{z_0^*} \tag{1}$$

where $\Delta r^* = 136.6$ mm and $r_0^* = 48.2$ mm, $\theta_0^* = 37.3$ mm and $z_0^* = 33.5$ mm are the innermost coating radius and the thickness, width and depth of the prepared voxel matrix, respectively.

The relative density across $\overline{r}^*$ based on the post-processed XRMCT data is given in Fig. 6. The total number of elements in each sublayer may be estimated using the relation

$$N_i^{elements} = \frac{16 \times 16 \times 2}{0.08^3} \times \rho_i^* \tag{2}$$

where ρ_i^* is the average relative density of sublayer number i. The relative density data presented in Fig. 6 indicates that the analyzed sublayer models had element counts in the range of 1,000,000 ($\rho^* = 1.0$) to 700,000 ($\rho^* = 0.7$).

3.4. Unit cell framework

While the yield surface of many metallic solids is defined by the equivalent von Mises stress, cellular and polymeric materials often show a strong dependence also of the pressure (i.e., the hydrostatic stress). Here, we will evaluate the pressure sensitivity of the global yield strength of each sublayer by numerical limit analyses based on a unit cell framework [21]. This framework enables an elaborate mapping of the global mechanical response of multi-phase materials that is not easily obtained from experiments. A prescribed stress state history is obtained through iterative monitoring and updating of the boundary conditions enforced on the unit cell model. By considering the sublayers as unit cells, which represent the properties of their respective region across the coating thickness, the pressure sensitivity of the yield strength as a function of the relative density can be numerically evaluated. As we are investigating initial yielding in this study, linear geometry has been used in all the analyses.

In the following, we adopt the notation from [21], where Σ_{ij} and σ_{ij} denote components of the global and local stress tensors, respectively. The local (continuum) stress σ_{ij} pertains to the individual elements in the model, which are assumed to be linearly elastic-perfectly plastic with yield stress equal to $\sigma_0 = 28$ MPa. Perfect plasticity is used because
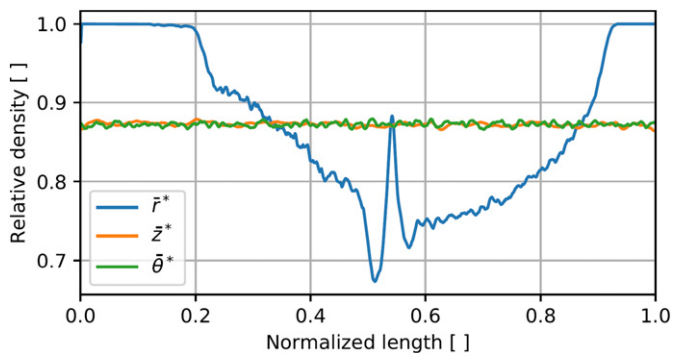

Fig. 6. The variation in relative density across the prepared voxel matrix for normalized dimensions $\overline{r}^*, \overline{\theta}^*$ and $\overline{z}^*$.

only the initial yield strength is evaluated here. Displacements that maintain a specified ratio between the stress components are applied to the exterior nodes. These are enforced via nonlinear multi-point constraints (MPC) between the unit cell nodes and a fictitious node outside the model. Throughout this work, we will impose proportional loading states, which corresponds to maintaining constant stress ratios. For details regarding the numerical procedure, the reader is referred to [26–29]. For each parallel edge-face pair, one node set is given symmetric boundary conditions, while the node set of the opposing boundary is displaced rigidly in the direction of the face normal. The displacement increments applied to each node set are calculated to meet the prescribed proportional loading conditions. The global stresses Σ_{ij} are calculated from the sum of the nodal forces recorded at the node sets divided by the nominal area of the undeformed boundary face. Each sublayer geometry is considered as a representative volume element (i.e., a unit cell) for the region. The global stress represents an averaged response measure where the interaction between the matrix behavior (governed by the local stresses) and the geometrical features of the sublayer is homogenized. With Σ_1, Σ_2, and Σ_3 denoting the ordered principal stress components ($\Sigma_1 > \Sigma_2 > \Sigma_3$), the hydrostatic stress (Σ_H) and the von Mises equivalent stress (Σ_{eq}^{VM}) are in turn calculated as

$$\Sigma_H = \frac{1}{3} (\Sigma_1 + \Sigma_2 + \Sigma_3) \tag{3}$$

and

$$\Sigma_{eq}^{VM} = \sqrt{\frac{1}{2} \left((\Sigma_1 - \Sigma_2)^2 + (\Sigma_2 - \Sigma_3)^2 + (\Sigma_3 - \Sigma_1)^2 \right)} \tag{4}$$

Initial global yielding is achieved when Σ_{eq}^{VM} reaches saturation. To describe the stress state, the stress triaxiality T and the Lode parameter L are introduced. These parameters are defined as

$$T = \frac{\Sigma_H}{\Sigma_{eq}^{VM}} \tag{5}$$

and

$$L = \frac{2\Sigma_2 - \Sigma_1 - \Sigma_3}{\Sigma_1 - \Sigma_3} \tag{6}$$

Proportional loading corresponds to constant values of T and L. The numerical simulations conducted herein will be restricted to a Lode parameter of $L = 1$ as it corresponds to generalized compression, which is believed to be the most important loading mode for the application of the pipeline. Using Eq. (6), $L = 1$ is seen to give $\Sigma_1 = \Sigma_2$. For each of the FE models (29 in total), 11 different global stress states corresponding to stress triaxialities of

$$T = \{-2.0, -1.0, -0.6, -0.3, -0.15, 0.0, 0.15, 0.3, 0.6, 1.0, 2.0\}$$

were analyzed. As already stated, the yield point of a stress state was evaluated from when the equivalent stress reached saturation, i.e., when there is no net increase of Σ_{eq}^{VM}

3.5. Numerical limit analysis results

Fig. 7(a) presents yield loci of the yellow colored sublayer meshes from Fig. 5(a). A clear trend is seen with respect to the position along the thickness direction. While the sublayers closest to the steel and the outer rim (i.e., the densest sublayers) show negligible pressure-dependency, the yield strength of the sublayers corresponding to the midmost regions of the coating is greatly influenced by the hydrostatic stress. These sublayers exhibit a decrease in the von Mises yield stress as the hydrostatic component decreases or increases in magnitude from its
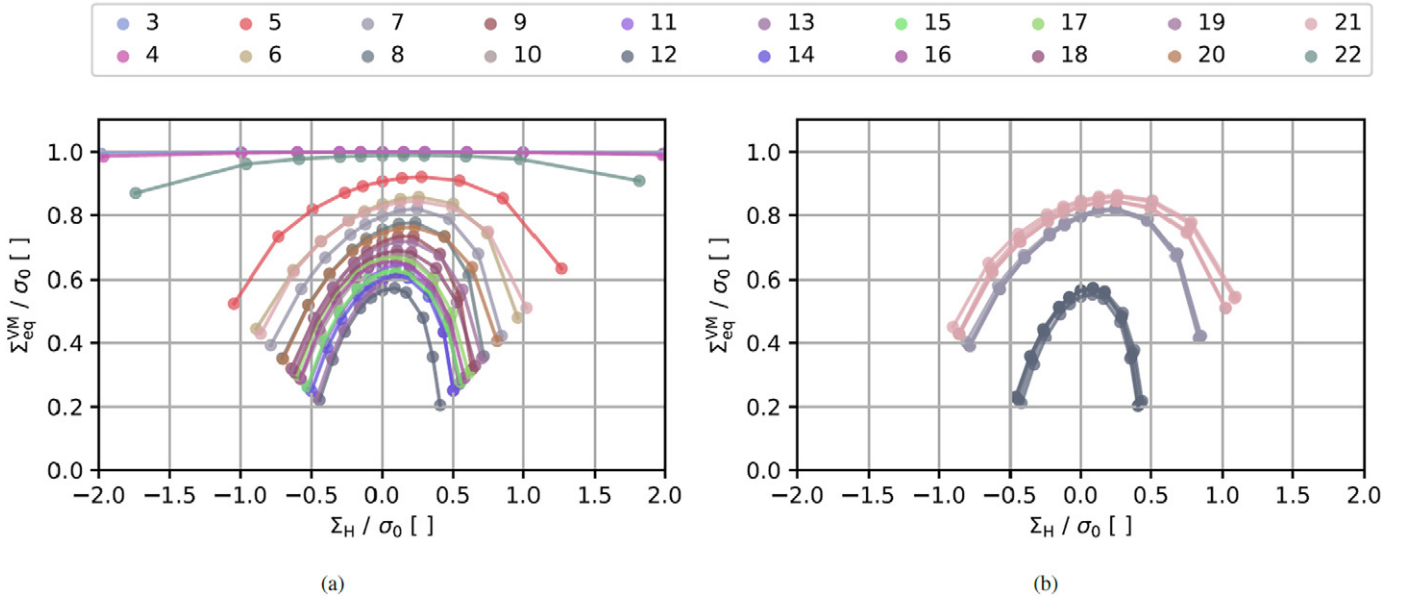
Fig. 7. Numerical yield loci of (a) a full quarter column of all sublayer models, and (b) all quarters of sublayers 7, 12 and 21 as presented in Fig. 5(a).

maximum. This bears resemblance to the response predicted by e.g. the Deshpande-Fleck model [18] or the Gurson model [16] for porous ductile solids. While the densities of these sublayers do not necessarily presuppose foam behavior, the initial yield response is seen to be comparable to such types of materials. An asymmetry around $\Sigma_H = 0$ is also clearly seen, which presumably results from morphology-induced anisotropy.

Simulations are also performed for the remaining quartiles of sublayer 7, 12 and 21 to study the consistency of the approach. The geometries of the remaining quartiles are shown in Fig. 5(a). Fig. 7 (b) presents the results from all quartiles of sublayer 7, 12, and 21, and demonstrates a low spread across the four geometries retrieved from each sublayer. The results indicate that the volumes are similar and can be considered representative for the purpose of this study.

4. Constitutive modeling

4.1. Formulation

The FE simulations in Section 3.4 resulted in an initial yield behavior typical for cellular materials. It was readily seen that the sublayers with the lowest relative density produce a stronger pressure-dependency than the denser layers. The XRMCT-based approach is, however, computationally expensive due to the large number of elements necessary to reflect the actual porous geometries of the different sublayers, which renders the approach intractable for simulating full-scale engineering problems. Thus, a homogenized continuum description is sought that reflects the main characteristics of the unit cell calculations. Such a model enables a quantification of the variation throughout the coating thickness in the simulation of larger components, such as impact on pipelines from anchors and trawl gear [6]. In the following, the proposed constitutive model of the coating is presented. The model corresponds to the Deshpande-Fleck model [18], which is a well-known plasticity model for cellular solids, however modified such that the pressure sensitivity is related to the porosity level.

A hypoelastic-plastic formulation is adopted and the rate-of-deformation tensor **D** is additively decomposed into elastic and plastic parts, viz.

$$\mathbf{D} = \mathbf{D}^e + \mathbf{D}^p \tag{7}$$

where $\mathbf{D}^e$ and $\mathbf{D}^p$ are the elastic and plastic rate-of-deformation tensors,

respectively. The rate-constitutive equations are assumed to be governed by the generalized Hooke's law, for which the elastic rate-of-deformation tensor reads

$$\mathbf{D}^e = \frac{1+\nu}{E}\boldsymbol{\sigma}^{\nabla GN} - \frac{\nu}{E}\text{tr}(\boldsymbol{\sigma}^{\nabla GN})\mathbf{I} \tag{8}$$

where $\boldsymbol{\sigma}^{\nabla GN}$ is the objective Green-Naghdi rate of the Cauchy stress tensor, **I** is the second-order unit tensor, E is the elastic modulus and ν is the Poisson ratio. The choice of $\boldsymbol{\sigma}^{\nabla GN}$ is due the VUMAT interface in Abaqus/Explicit. The elastic modulus, E_{PP}, and the Poisson ratio ν_{PP} of the polypropylene were calibrated to 800 MPa and 0.4, respectively, by Vestrum et al. [9]. The elastic parameters depend upon the porosity of cellular materials [7], and they are consequently assumed to scale according to the linear relations

$$E(f) = (1-f)\,E_{PP} \tag{9}$$

and

$$\nu(f) = (1-f)\,\nu_{PP} \tag{10}$$

where the porosity f is defined in terms of the relative density ρ^* by

$$f = 1 - \rho^* \tag{11}$$

The plastic rate-of-deformation tensor is defined by the associated flow rule as

$$\mathbf{D}^p = \lambda \frac{\partial \Phi}{\partial \boldsymbol{\sigma}} \tag{12}$$

where λ is the plastic multiplier and Φ is the yield function. Green [17] presented a yield function for porous solids later reformulated by Deshpande and Fleck [18] as

$$\Phi = \sigma_{eq}^{DF} - \sigma_y \tag{13}$$

where

$$\sigma_{eq}^{DF} = \sqrt{\frac{1}{\left(1+(\alpha/3)^2\right)}\left[\left(\sigma_{eq}^{VM}\right)^2 + (\alpha\sigma_H)^2\right]}. \tag{14}$$

Here, σ_y is the yield stress and α is the pressure sensitivity parameter, while σ_{eq}^{VM} and σ_H are in turn the von Mises equivalent stress and the hydrostatic stress defined by

$$\sigma_{eq}^{VM}(\boldsymbol{\sigma}) = \sqrt{\frac{3}{2}\boldsymbol{\sigma}':\boldsymbol{\sigma}'}, \quad \sigma_H(\boldsymbol{\sigma}) = \frac{1}{3}\text{tr}(\boldsymbol{\sigma}) \tag{15}$$

where $\boldsymbol{\sigma}$ denotes the Cauchy stress tensor and $\boldsymbol{\sigma}' = \boldsymbol{\sigma} - \sigma_H\mathbf{I}$ defines the stress deviator. Yielding occurs under the condition $\Phi = 0$, which defines the yield surface. The loading-unloading conditions in Kuhn-Tucker form are given by

$$\Phi \leq 0, \quad \lambda \geq 0, \quad \lambda\Phi = 0 \tag{16}$$

and the consistency condition is given by

$$\lambda\dot{\Phi} = 0. \tag{17}$$

Using the associated flow rule given in Eq. (12) and the equivalence in plastic power, i.e., $\boldsymbol{\sigma}:\mathbf{D}^p = \sigma_y p$, it can then be shown that $p = \lambda$, where p is the equivalent plastic strain rate conjugate to the yield stress σ_y.

4.2. Yield surface calibration

Deshpande and Fleck [18] introduced the relation in Eq. (14) as a phenomenological isotropic model for the plastic behavior of aluminum foams, but the model has since become a prevailing plasticity model for different cellular materials. The yield surface is a quadratic function in the stress space (σ_{eq}^{VM}, σ_H), and the shape and the size of the surface are governed by the two parameters α and σ_y, respectively. As the results from the unit cell simulations indicated that the behavior of the coating is anisotropic, the isotropic constitutive model is an approximation and will not produce a perfect fit to the data. The constitutive model is calibrated based on the results of the FE unit cell analyses of the different sublayers and modified to allow for an evolution of the yield surface as the density (or porosity) of the material changes. The global stress state represented by Σ_{ij} in the unit cell analyses corresponds to the stress state σ_{ij} in a homogenized continuum description of the corresponding region. The yield function Φ in Eq. (13) is accordingly calibrated to the computed stress states (Σ_{eq}^{VM}, Σ_H) at yielding of each

sublayer evaluation using a least-square fitting approach. This produces 20 unique sets (one for each sublayer) of σ_y and α. Fig. 8(a) presents the results from the calibration of the yield function to the unit cell data for each sublayer. We see some deviations between the analytical yield function and the unit cell data. This is mainly because a symmetric yield function is fitted to the asymmetric unit cell data, but the correspondence is generally good.

The values of α and σ_y obtained from the calibration procedure are plotted against the porosity f in Fig. 8(b). Both parameters show a strong and clear correlation with the average porosity of the sublayer regions. This variation can be reflected in the yield function by expressing the pressure sensitivity parameter α and the yield stress σ_y as functions of the porosity f. The dotted lines in Fig. 8(b) correspond to the fitted empirical relations

$$\alpha = \alpha(f) = b_1 f^{b_2} \tag{18}$$

with $\{b_1, b_2\} = \{2.03, 0.45\}$ and

$$\sigma_y = \sigma_y(f) = \sigma_0 \exp(c_1 f) \tag{19}$$

where $\sigma_0 = 28$ MPa and $c_1 = -2.458$. These expressions for the pressure sensitivity parameter and the yield stress will be used in the Deshpande-Fleck yield function (Eq. (13)) in the sequel.

4.3. Evolution of porosity

The porosity f evolves with the deformations imposed to the material. Compression of the coating (i.e., negative volumetric strain) will result in compaction of the pores and an intricate interaction between the internal surfaces when the pores are fully compacted. Tensile loading will facilitate expansion of the pores. The porosity f clearly changes the overall yield strength of the coating, and the yield surface is indeed a function of the evolving porosity. If we assume that the elastic strains are negligible compared to the plastic strain, and that the matrix exhibits plastic incompressibility, it can be shown that the porosity evolution may be expressed as

$$\dot{f} = (1-f)\,\text{tr}(\mathbf{D}^p) = (1-f)\lambda\frac{\alpha^2\sigma_H}{\sigma_{eq}^{DF}\left(1 + (\alpha/3)^2\right)} \tag{20}$$
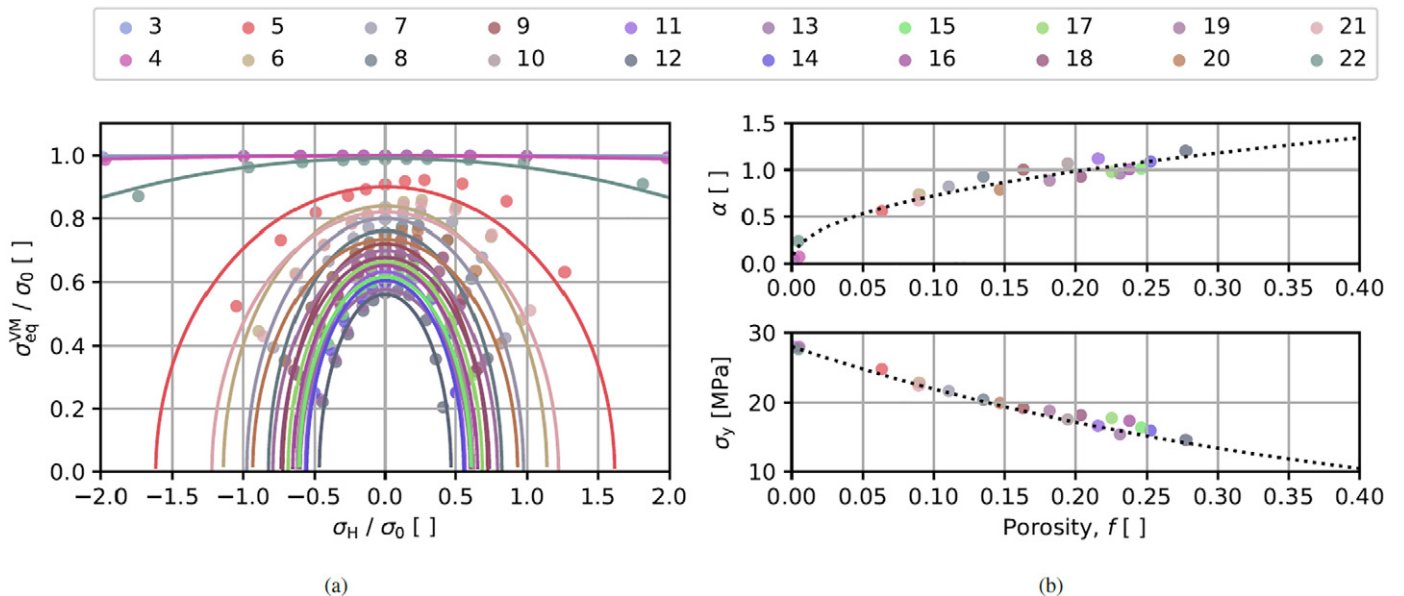

Fig. 8. Plots of (a) the analytical yield surfaces calibrated to the yield points produced by the unit cell simulations and (b) the pressure sensitivity parameter and the yield stress as functions of the average porosity of the corresponding sublayer. The two figures share the legend printed above.

where the latter expression is obtained using Eq. (12). A negative increment in the plastic volumetric strain, hence compaction, will produce a reduction in porosity. The reduced porosity will result in increased hardening and lower pressure sensitivity in the plastic response of the coating by lowering α and increasing σ_y, and the Deshpande-Fleck yield function in Eq. (13) thus approaches the von Mises yield function. On the contrary, positive volumetric plastic strain increases the average porosity, and consequently increases α and lowers σ_y, such that the yield function becomes increasingly pressure sensitive and the overall yield strength is lowered.

4.4. Implementation

The constitutive model presented herein was implemented as a material user subroutine (VUMAT) in Abaqus/Explicit [22], in which a cutting-plane return mapping algorithm was used to integrate the constitutive equations. The updates of $\alpha(f)$ and $\sigma_y(f)$ were explicit, i.e., the value of f from the previous increment was used in the return mapping. The effect of this explicit update is deemed to be negligible due to the very small strain increments provided to the material subroutine in the explicit FE solver.

5. Validation of constitutive model

5.1. Specimens

A validation study was performed where the proposed constitutive model was used to simulate the response of three through-thickness coating specimens tested under nominal uniaxial compression. XRMCT was used to map the internal porosity throughout the thickness of the specimens (i.e., along the r axis) prior to testing. The mapped porosity variation was used to assign the initial material properties (based on the previous calibration of α and σ_y) of 24 sublayers across the specimens during the numerical simulations. Finally, the numerical results were compared to the experimental results. The nominal measurements of the specimens' thickness, width and depth were approximately 48 mm, 40 mm and 40 mm, respectively. Exact measurements were used in the FE model of each individual specimen. All specimens span across all coating layers and thus had a curved face at the initial interface between the coating and the steel pipe, and at the outer rim of the coating.

5.2. Experimental

The approach for XRMCT acquisition and remapping described in Section 3 was applied to the specimens. From this, binary voxel matrices were produced such that the variation in porosity along the r axis of the specimens could be evaluated, which are presented in Fig. 9. Fig. 9 also shows the porosity profile across the sublayer regions to be used as input in the proposed constitutive model for the pipeline

coating. Apart from a difference in extreme values around $\bar{r}^* \approx 0.5$, the porosity profiles are seen to be comparable between the specimens. Specimen 03 is found to have a slightly larger maximum porosity than Specimen 02, both in terms of actual and sublayer porosity, whereas Specimen 01 exhibits intermediate values. The difference in maximum sublayer porosity is as large as $\Delta f = 0.05$ between Specimen 02 and Specimen 03. Note that information about the actual maximum porosity is lost due to the averaging of porosity across this highly fluctuating sublayer. These extrema may be of significance as it is expected that the deformation localizes in the weakest sublayers (i.e., highest porosity) at initial yield.

All three specimens were tested in nominal uniaxial compression under quasi-static conditions in an Instron 5982-L2035 test machine [30]. To represent realistic boundary conditions, a steel mount with a curved face for the specimens to be placed on during testing was produced. The steel mount had a radius equal to the outer cross-section radius of the original steel pipeline. A 100kN Instron 2580-301 load cell, mounted between the test machine crosshead and the machine-specimen interface, recorded the reaction force F during testing. In synchronization with the force readings, a camera recorded still images of the specimen and parts of the test machine. A patch with a checkerboard pattern was glued to the machine crosshead close to the machine-specimen interface. The displacement of the pattern was traced using point-tracking available in the in-house DIC-software eCorr [31] and used as a measure of the machine displacement u when the results were post-processed.

5.3. Numerical

The compression tests were analyzed using Abaqus/Explicit and the model setup is shown in Fig. 10. Both the machine interface and mount were modeled as analytical surfaces, while the analyzed specimen was modeled using linear solid elements with reduced integration. The specimen was partitioned along its radial dimension at 2 mm intervals, which is illustrated by the differently colored layers in Fig. 10. Each unique color corresponds to a homogenized region modeled by the constitutive model presented in Section 4 with its initial parameters (α and σ_y) given by the average porosity f across the corresponding region in the XRMCT scan. Note that each sublayer has a single initial porosity, although the porosity throughout each sublayer, in the actual specimen, naturally varies.

5.4. Validation results

Fig. 11 presents the force-displacement curves from the three uniaxial compression tests and the results from the FE simulations using the proposed constitutive model. The simulations are seen to produce force levels that are indeed in reasonable agreement with the actual response. However, the simulations give a slightly stiffer initial response and the force level is initially overestimated compared to the
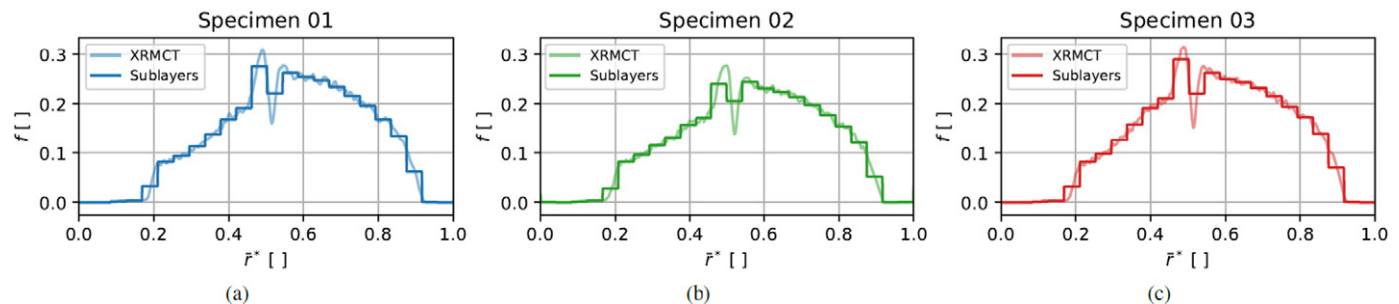

Fig. 9. Porosity f along the dimensionless $\bar{r}^*$ axis for each of the three specimens: (a) Specimen 01, (b) Specimen 02 and (c) Specimen 03. The graphs labeled "XRMCT" represent the porosity estimated with high-resolute XRMCT data, whereas the jagged graphs labeled "Sublayers" represent the averaged porosities across 24 sublayers.
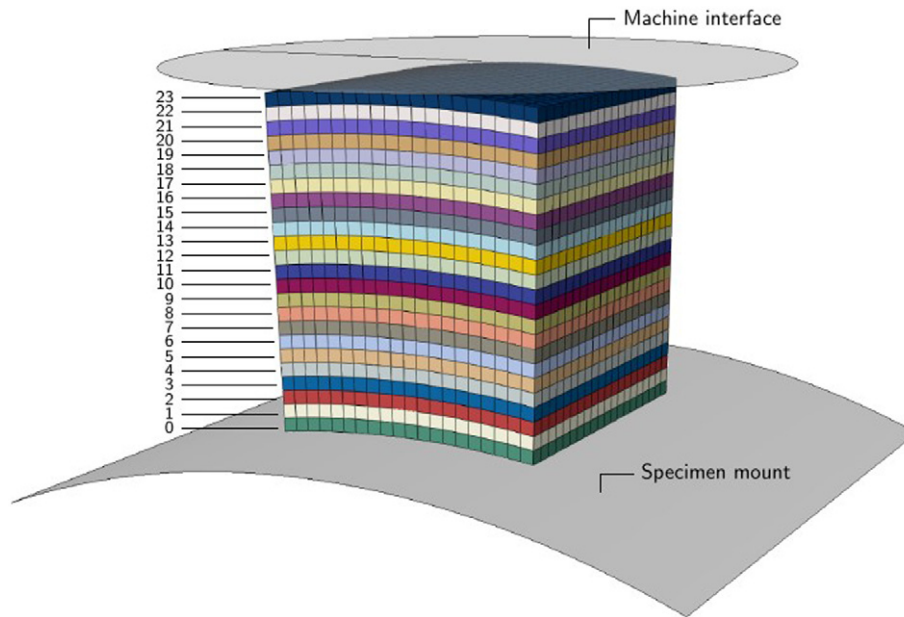
Fig. 10. Overview of the assembled model in Abaqus consisting (from top to bottom) of the test machine interface (flat analytical surface), specimen (meshed solid) and specimen mount (curved analytical surface). The different sublayers are labeled and highlighted with different colors.

experiments. Possible reasons for these differences may be a too simplistic linear relation assumed for the elastic stiffness (Eq. (9)) and an overestimation of the initial yield strength. The latter could be related to the heterogeneity of the porosity in each sublayer, which would render some regions with somewhat low porosity. These results were expected from the results in Fig. 9. If the number of sublayers across the thickness is increased, this spatial heterogeneity of the porosity in each sublayer would be reduced. The force level would thus be lowered and in better correspondence to the experimental data. Also, the proposed model is calibrated based on the assumption that the constituent polypropylene material has a perfectly plastic behavior with yield stress ($\sigma_0 = 28$ MPa) retrieved from the materials data sheet. Johnsen et al. [32] studied the initial yield stress of a polypropylene material produced by Borealis and used in pipeline coatings. They found that by going from a temperature of 0°C to 25°C, the initial yield stress in compression at approximately quasi-static strain-rates was reduced from around 38 MPa to 24 MPa. While the solid layer constitutes only a minor part of the full coating, these results illustrate that the mechanical behavior of polypropylene is temperature dependent. The compression tests were done at room temperature which varied between 22°C and 25°C. It is reasonable to assume that this phenomenon may partly cause the

deviations seen at initial yielding. A mismatch is also observed in terms of hardening at large deformations. The proposed constitutive model does not include any hardening of the polypropylene microstructure, which may explain the deviations observed at large deformations. Other potential sources of error are deviations between the specimen geometries and model geometry, and inaccurate modeling of the machine-specimen boundary conditions.

Despite the differences observed between the FE simulations and the experimental results, the main trends are well captured by the constitutive model. It is argued that the discrepancies observed at the various stages of deformation could be compensated for by a more advanced constitutive model of the polypropylene (i.e., through micro-mechanical modeling). Thus, the developed model is deemed to be a good starting point for further developments aimed at improving the response in the initial and last stages of the deformation.

6. Concluding remarks

This work has addressed the constitutive modeling of a graded porous polymer pipeline coating based on X-ray micro computed tomography (XRMCT). A specimen of the coating was scanned using XRMCT and the
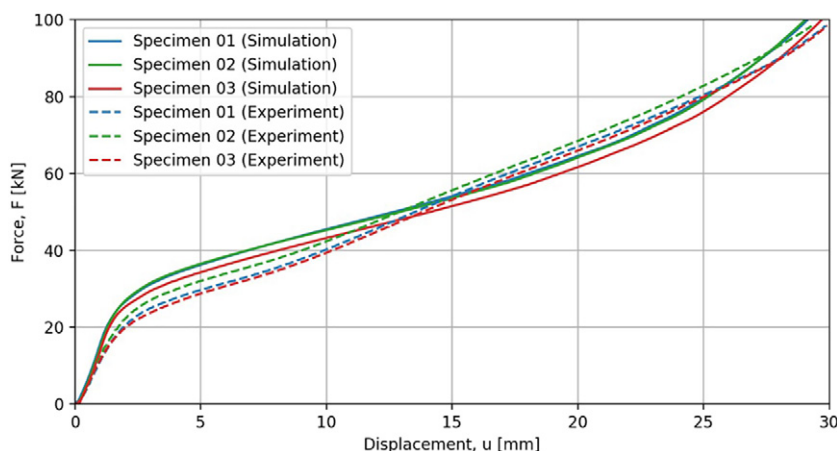

Fig. 11. Comparison between numerical results produced using the constitutive model and the experimental results.

post-processed imaging data has been used to generate FE models of the polymer coating, thus enabling a detailed numerical study of the mechanical response using only basic material information about the polymer matrix as input. The numerical results from these FE models served as a basis for modifying an existing constitutive model to reflect the variation of the averaged porosity across the thickness of the polymer coating.

The main results from the work are summarized below.

i. An approximately 48 mm × 35 mm × 40 mm large multi-layer coating sample was scanned using XRMCT, enabling detailed mapping of the macroscopic morphology of the porous coating.

ii. The XRMCT data was divided into 24 sections (or sublayers) across r to produce volumes of different macroscopic morphologies. The sublayers were converted into FE models, which were analyzed using a unit cell modeling framework to obtain the yield locus of each sublayer in generalized compression. The pressure sensitivity of the yield locus was seen to vary significantly across the radius r.

iii. The Deshpande-Fleck yield function was individually calibrated to the yield loci of the sublayers with good accuracy. The yield function parameters were found to be strongly correlated to the porosity of the sublayers. A constitutive model was developed and implemented as a user-subroutine in Abaqus/Explicit where the Deshpande-Fleck yield function parameters were expressed as functions of porosity, and the porosity evolves with the plastic volumetric strain. The constitutive model allows for the coating to be included in simulations of large-scale components.

iv. The constitutive model was validated through an experimental study where 3 coating specimens were scanned using XRMCT and tested in uniaxial compression. The porosity variation along the radius r for each specimen was used as input to the constitutive model when simulating the uniaxial compression tests. The force-displacement curves produced from the simulations were compared with those from the experiments. The model was found to capture the main trends well, but the need for a more sophisticated constitutive model for the polypropylene was revealed. However, the proposed modeling framework produced satisfying results when compared with experiments and was deemed as a good starting point for further development.

Through this work, we have shown that it is possible to produce a constitutive model for porous polymeric coating materials by simply evaluating the macroscopic pore morphology using XRMCT. The proposed model will potentially serve as a computationally efficient and cost-effective means of simulating the behavior of similar coatings to a full pipeline design subjected various loading situations.

Credit author statement

Vestrum: manuscript, experimental and numerical work; Dæhli: unit cell simulations, manuscript; Børvik/Hopperstad: manuscript, discussions, supervision.

Declaration of competing interest

The authors declare that they have no known competing financial interests or personal relationships that could have appeared to influence the work reported in this paper.

Acknowledgment

Data availability statement

The raw data required to reproduce these findings cannot be shared at this time as the data also forms part of an ongoing study. The processed data required to reproduce these findings cannot be shared at this time as the data also forms part of an ongoing study.

References

[1] G.P. Guidetti, G.L. Rigosi, R. Marzola, The use of polypropylene in pipeline coatings, Progress in Organic Coatings 27 (1–4) (1996) 79–85January-April.

[2] DNV, DNV-OS-F101 Submarine Pipeline Systems, October 2013 (Offshore Standard).

[3] E. Legghe, Y. Joliff, L. Belec, E. Aragon, A. Margaillan, Computational analysis of internal stresses generated during the manufacturing process of a monolayer or three-layer pipeline coating, Comput. Mater. Sci. 48 (2) (2010) 360–365April.

[4] M.R. Tchoquessi Diodjo, Y. Joliff, L. Belec, E. Aragon, F.X. Perrin, M. Bonnaudet, L. Lanarde, Numerical modeling of stresses relaxation phenomena in the complex assembly steel pipe/three layers polyethylene coating, Progress in Organic Coatings 90 (2016) 54–82.

[5] J. Zhao, Q. Zhao, C. Wang, B. Guo, C.B. Park, G. Wang, High thermal insulation and compressive strength polypropylene foams fabricated by high-pressure foam injection molding and mold opening of nano-fibrillar composites, Mater. Des. 131 (2017) 1–11.

[6] O. Vestrum, M. Kristoffersen, M.A. Polanco-Loria, H. Ilstad, M. Langseth, T. Børvik, Quasi-static and dynamic indentation of offshore pipelines with and without multi-layer polymeric coating, Mar. Struct. 62 (2018) 60–76.

[7] L.J. Gibson, M.F. Ashby, Cellular Solids: Structures and Properties, 2. edition, Cambridge Solid State Science Series, , Cambridge University Press, 1997.

[8] A. Reyes, T. Børvik, Quasi-static behaviour of crash components with steel skins and polymer foam cores, Materials Today Communications 17 (2018) 541–553.

[9] O. Vestrum, M. Langseth, T. Børvik, Finite element modeling of porous polymer pipeline coating using X-ray micro computed tomography, Composites Part B 172 (2019) 406–415.

[10] C. Petit, E. Maire, S. Meille, J. Adrien, Two-scale study of the fracture of an aluminum foam by X-ray tomography and finite element modeling, Mater. Des. 120 (2017) 117–127.

[11] E. Maire, A. Fazekas, L. Salvo, R. Dendievel, S. Youssef, P. Cloetens, J.M. Letang, X-ray tomography applied to the characterization of cellular materials. Related finite element modeling problems, Compos. Sci. Technol. 63 (2003) 2431–2443.

[12] E. Maire, P.J. Withers, Quantitative X-ray tomography, Int. Mater. Rev. 59 (2014).

[13] J.A. Elliott, A.H. Windle, J.R. Hobdell, G. Eeckhaut, R.J. Oldman, W. Ludwig, E. Boller, P. Cloetens, J. Baruchel, In-situ deformation of an open-cell flexible polyurethane foam characterised by 3D computed microtomography, J. Mater. Sci. 37 (2002) 1547–1555.

[14] S. Youssef, E. Maire, R. Gaertner, Finite element modelling of the actual structure of cellular materials determined by X-ray tomography, Acta Mater. 53 (2005) 719–730.

[15] D.C. Drucker, W. Prager, Soil mechanics and plastic analysis or limit design, Q. Appl. Math. 10 (1952) 157–165.

[16] A.L. Gurson, Continuum theory of ductile rupture by void nucleation and growth: part I—yield criteria and flow rules for porous ductile media, Journal of Engineering Materials 99 (1977) 2–15, https://doi.org/10.1115/1.3443401. January.

[17] R.J. Green, A plasticity theory for porous solids, Journal of the Mechanics and Physics of Solids, International Journal of Mechanical Sciences 14 (1971) 215–224.

[18] V.S. Deshpande, N.A. Fleck, Isotropic constitutive models for metallic foams, Journal of the Mechanics and Physics of Solids 48 (2000) 1253–1283.

[19] R. von Mises, Mechanik der Festen Korper im Plastisch Deformablen Zustand, Nachrichten von der Gesellschaft der Wissenschaften zu Gottingen 1913, pp. 582–592.

[20] F. Fritzen, S. Forest, T. Böhlke, Computational homogenization of porous materials of Green type, Comput. Mech. 52 (2013) 121–134.

[21] L.E.B. Dæhli, O.S. Hopperstad, A. Benallal, Effective behaviour of porous ductile solids with a non-quadratic isotropic matrix yield surface, Journal of the Mechanics and Physics of Solids 130 (2019) 56–81.

[22] Abaqus, https://www.3ds.com/products-services/simulia/products/abaqus/, Accessed date: 1 December 2019.

[23] Shawcor Norway, https://www.shawcor.com/locations/plants/europe/orkanger-norway, Accessed date: 1 December 2019.

[24] Polypropylene BA202E, https://www.borealisgroup.com/product/ba202e/, Accessed date: 1 December 2019.

[25] J. Andersons, M. Kirpluks, L. Stiebra, U. Cabulis, Anisotropy of the Stiffness and Strength of Rigid Low-density Closed-cell Polyisocyanurate Foams, 92, 2016 836–845.

[26] L.E.B. Dæhli, J. Faleskog, T. Børvik, O.S. Hopperstad, Unit cell simulations and porous plasticity modelling for strongly anisotropic FCC metals, European Journal of Mechanics A/Solids 65 (2017) 360–383.

[27] Z.G. Liu, W.H. Wong, T.F. Guo, Void behaviors from low to high triaxialities: transition from void collapse to void coalescence, Int. J. Plast. 84 (2016) 183–202.

[28] J. Kim, X. Gao, T.S. Srivatsan, Modeling of void growth in ductile solids: effects of stress triaxiality and initial porosity, Eng. Fract. Mech. 71 (2004) 379–400.

[29] J. Faleskog, X. Gao, C.F. Shih, Cell model for nonlinear fracture analysis – I. micromechanics calibration, Int. J. Fract. 89 (1998) 355–373.

[30] Instron, 5980 floor model systems for high-capacity universal testing, http://www.instron.us/en-us/products/testing-systems/universal-testing-systems/electromechanical/5900/5980-floor-model, Accessed date: 1 August 2019.

[31] E. Fagerholt, eCorr digital image correlation, https://www.ntnu.edu/kt/ecorr, Accessed date: 1 August 2019.

[32] J. Johnsen, F. Grytten, O.S. Hopperstad, A.H. Clausen, Influence of strain rate and temperature on the mechanical behaviour of rubber-modified polypropylene and cross-linked polyethylene, Mech. Mater. 114 (2017) 40–56.